Turkish Journal of Engineering
https://dergipark.org.tr/en/pub/tuje
e-ISSN 2587-1366

Effective adsorption of malachite green with silica gel supported iron-zinc bimetallic nanoparticles

Memduha Ergüt [*1], **Ayla Özer** [2]

[1] *Sivas University of Science and Technology, Department of Chemical Engineering, Türkiye, memduha.ergut@gmail.com*
[2] *Mersin University, Department of Chemical Engineering, Türkiye, ayozer@mersin.edu.tr*

Cite this study: Ergüt, M., & Özer, A. (2024). Effective adsorption of malachite green with silica gel supported iron-zinc bimetallic nanoparticles. Turkish Journal of Engineering, 8 (3), 510-523

https://doi.org/10.31127/tuje.1413970

Keywords
Adsorption
Malachite green
Bimetallic nanoparticles
Silica gel
Composite material

Research Article

Received: 03.01.2024
Revised: 19.02.2024
Accepted: 21.02.2024
Published: 05.07.2024

Abstract

In the present study, a composite material consisting of silica gel 60 supported iron-zinc bimetallic nanoparticles (Si/Fe-ZnNPs) was prepared and characterized by SEM, EDX, FTIR, and XRD analysis. The adsorbent properties of the synthesized composite material were evaluated with the removal of Malachite Green (MG). According to characterization results, the cubic structures and agglomerated nano-sized spherical particles (≈30 nm) were formed. The FT-IR spectrum confirms the formation of Fe-Zn NPs through the observation of the Fe-O stretches and metal-metal stretching vibrations of (Zn^{2+} – O^{2-}) adsorption bands. Additionally, the FT-IR revealed the presence of Si-O-Si, Si-O-H stretching, and O-Si-O bending vibrations attributed to silica gel 60. The optimal environmental conditions for adsorption were determined to be a natural pH of 3.3, an adsorption temperature of 50°C, and an adsorbent concentration of 1.0 g/L. An increase in equilibrium uptakes of MG was observed with a linear correlation to initial dye concentrations. Thermodynamic studies indicated that the adsorption process was endothermic, non-spontaneous, and increasing disorder at the solid-solution interface during adsorption with positive ΔH, ΔG, and ΔS values, respectively. The experimental results revealed that the Langmuir isotherm model provided the best fit for the equilibrium data. The maximum monolayer coverage capacity of Si/Fe-ZnNPs was 666.67 mg/g at an optimum temperature of 50°C. Further analysis displayed that the kinetic adsorption data adhere to the pseudo-second-order kinetic model. Additionally, Weber-Morris model results revealed the effectiveness of both the film and intra-particle diffusion in the adsorption.

1. Introduction

Today, the escalating worldwide contamination of natural water from chemicals is a foremost challenge that humanity confronts as it produces considerable and unpredictable short and long-term impacts on aquatic life and human well-being [1]. The most important sources of water pollution are industrial chemicals, pesticides, fertilizers, oil sludge, and radioactive, solid, and commercial wastes. The common source of water pollution is human activity, although some natural and anthropogenic sources can cause it [2]. Many pollutants with adverse health effects such as textile dyestuffs, pesticides, pharmaceutical compounds, plasticizing agents, disinfection by-products, polychlorinated biphenyls, and polycyclic aromatic hydrocarbons have been determined in wastewater discharge [3].

Textile dyestuffs have attracted huge attention because of potential health and environmental hazards. Dyes possess intricate molecular structures that include chromophores and auxochromes. Chromophores are accountable for the color of the dye, while auxochromes comprising -NH_3, -COOH, -HSO_3, or -OH groups control the tint's intensity and make the molecule soluble in water [4]. The yearly global production of dyes surpasses $7x10^5$ tonnes, and industrial pollutants expel 10-15% of them into water sources. Even at a concentration of only 1 mg/L, dyes and their intermediates are the main and most dangerous pollutants found in the effluent produced by the textile industry [5].

Malachite green (MG) is a cationic dye that belongs to the triphenyl methane family. It is one of the most widely used industrial dyes in the manufacturing industries such as textile, paper, and food processing. Its uncontrolled discharge brings about harmful effects on the aquatic environment and human health due to its toxic, cancerogenic, and mutagenic characteristics [6].

Different treatment methods such as adsorption, ion exchange, electrochemical, catalysis, ozonation, reverse osmosis, coagulation, chemical precipitation, membrane filtration, and biological process techniques have been used for discharging dyestuffs from wastewater [7]. Adsorption is still a well-known treatment method owing to its being cost-effective, ease of operation, high removal performance, and environment-friendly nature [8].

As a consequence of rapid developments in the field of nanotechnology, the number of studies on the use of reusable, highly efficient, and low-cost nanoparticles as an adsorbent due to their large specific surface areas are increasing. Nanomaterials have many advantages, such as low diffusion resistance, easy access to the reactants, and a large number of active centers due to their large surface area [9]. Bimetallic nanoparticles prepared by adding other metal-based materials to iron-based nanoparticles to increase the adsorption capacity of them show more effective properties compared to mono-metallic ones. Moreover, their nanostructure and magnetic properties contribute to adsorption performance collectively and synergistically in the treatment of various contaminants such as dyestuffs, phenolics, pharmaceuticals, and heavy metals [10].

Various iron-based bimetallic nanoparticles have been reported as adsorbents. It has been indicated that the addition of a second catalytic metal such as Zn, Ag, Ni, Cu, or Pd may enhance the adsorption rate compared to using iron nanoparticles alone [11]. Additionally, incorporating bimetallic nanoparticles onto solid supports such as SiO_2, activated carbon, multi-walled carbon nanotube, zeolite, alginate, hydroxyapatite, chitosan, and gum can enhance the mechanical robustness and enhance the uptake of adsorbent [12].

Several iron-based materials, including zero-valent iron nanoparticles (nZVI FeNPs) [13–15], iron-containing bimetallic nanoparticles such as Fe/Ni-NPs [16–18], Fe/Zn-NPs [11, 19], and Fe/Cu–NPs [20, 21] as well as porous materials containing iron, like zeolites, clays, activated carbon, carbon nanotubes, graphene-based materials, biochar, mesoporous silica and metal-organic frameworks (MOFs) have been tested as effective adsorbents for the removal of different types of textile dyestuffs [22–24].

Kumar et al. synthesized bimetallic Fe–Zn nanoparticles via a co-precipitation method and used them for the adsorptive removal of carcinogenic dye malachite green and Congo red. The Langmuir maximum adsorption capacity for MG and CR was found to be 21.74 and 28.56 mg/g, respectively [11].

Silica comes from a variety of sources including fumed silica, sodium metasilicate, silica gel, and tetraethyl orthosilicate [25]. Silica gel is a type of amorphous synthetic silica. It is a hydrophilic mesoporous material and is mainly composed of SiO_2. It is a rigid, continuous network of colloidal silica connected to very small grains of hydrated SiO_2. It is non-hazardous, low cost, and has a specific surface area of about 100-1000 m^2/g. Porous silica gels are widely used as adsorbent materials in various applications such as adsorption, cooling, dehumidification, gas separation, and desalination [26]. Moreover, mesoporous silica gel has wide applications as a catalyst and catalytic support due to its outstanding surface properties and porosities, which are higher than those of zeolites and clays [27]. Additionally, silica gel has been used as an adsorbent for treating wastewater due to its stability, large pore channels, possible reuse, lower price, excellent chemical stability, high surface area, and high mechanical resistance [28, 29]. The surface of silica gel exhibits high chemical reactivity due to the presence of silanol groups (Si-OH). Additionally, the large pore channels enable selective adsorption of specific pollutants [30]. Silica materials are considered effective adsorbents for cationic dye removal owing to hydrogen bonding with silanol groups allowing cationic and non-ionic surfactants to adsorb onto the silica surface [27]. Many studies have reported that styryl pyridinium dyes are adsorbed on the silica gel surface [31].

Several studies have been reported on the synthesis of silica-based adsorbents and the adsorption of MG. Mansa et al. carried out the preparation of modified silica NPs for MG adsorption [32]. In the study of Hasan-Zadeh et al. acid modified silica nanoparticles were employed for the treatment of MG in wastewater. The material has a diameter of approximately 20.12 nm and a pore volume of around 1.04 cm^3/g. The adsorption capacity was determined to be 116.3 mg/g at optimum pH 6.5, 10 mg/L initial dye concentration, and 60 min equilibrium time. The adsorption performance indicated that the process of MG adsorption may occur on a multilayer porous material [33].

Abderrahman [25] synthesized different zeolite nanostructures from waste aluminum cans by hydrothermal method using different silicon sources. The zeolite nanostructures were synthesized using fumed silica (ZF), sodium metasilicate (ZM), silica gel (ZS), and tetraethyl orthosilicate (ZT). The prepared zeolite nanostructures were utilized in the removal of MG dye from aqueous media. The maximum adsorption capacities (mg/g) of MG dye on (ZF, ZM, ZS, and ZT) adsorbents were reported as 226.757, 239.234, 29.744, and 25.221, respectively.

Samiey and Toosi [31] investigated the adsorption of MG on silica gel under varying conditions, including temperature (308-328 K), pH, NaCl concentration, and binary mixtures of 2-propanol with water. The maximum adsorption capacity was found to be 39.7 mg/g.

To our knowledge, no study has been reported so far on the synthesis of silica gel supported iron-zinc bimetallic nanoparticles (Si/Fe-Zn NPs) composite material and its use as an adsorbent in MG removal from aqueous media. The study aims to synthesize a useful composite material with a high adsorption capacity for MG through a combination of silica gel and Fe-ZnNPs.

Therefore, the purpose of this study was to synthesize and characterize a composite material consisting of silica gel 60 supported Fe-Zn bimetallic nanoparticles, and to investigate its effectiveness as an adsorbent in treatment of MG. The characterizations of the synthesized Si/Fe-ZnNPs were carried out using XRD, FTIR, SEM, and EDX analysis methods. Subsequently, the Si/Fe-ZnNPs were tested as an adsorbent for MG treatment in a batch adsorption system. The study examined the effects of environmental conditions such as adsorbent concentration, initial dye concentration, and

temperature. The research also investigated the adsorption thermodynamics, and modeling studies of equilibrium, kinetic, and mass transfer for MG adsorption.

2. Method

2.1. Materials

$FeCl_3.6H_2O$ (≥98.0%), $ZnCl_2.4H_2O$ (≥98.0%), Malachite Green oxalate (C.I. 42000), and NaOH (pellets, anhydrous, ≥99%) were provided from Merck. Silica gel (Silica gel 60 (SiO_2), for column chromatography, mean pore diameter 60 Å, 63–200 µm, spherical) was acquired from Sigma Aldrich. MG was obtained in its commercial pure form. It is a cationic type with a molecular weight of 365 g/mol and a maximum absorption wavelength (λmax) of 618 nm. Its chemical structure is depicted in Figure 1, [34].

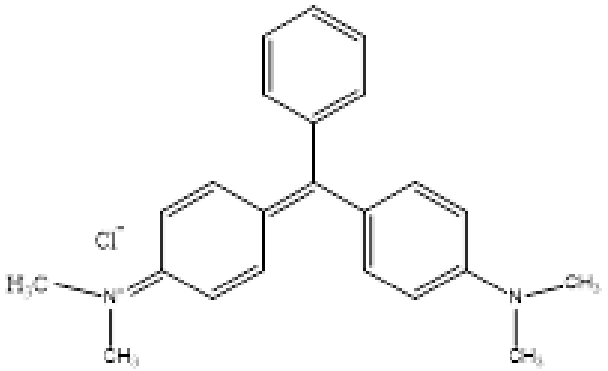

Figure 1. The molecular structure of Malachite Green.

2.2. Synthesis of composite material

Silica gel supported iron-zinc bimetallic nanoparticles composite material was synthesized by chemical co-precipitation and impregnation methods. Firstly, Fe-Zn bimetallic nanoparticles were produced through the chemical co-precipitation technique and silica gel 60 was mixed with the Fe-Zn bimetallic nanoparticles (Fe-ZnNPs) using the impregnation method. Fe-ZnNPs were prepared according to the procedure reported previously by Kaya et al. At room temperature, 25 mL of 0.4 M $FeCl_3.6H_2O$ and 25 mL of 0.2 M $ZnCl_2.4H_2O$ were mixed for 15 minutes. The solution's pH of 11 was adjusted by the inclusion of 25 mL of 3.0 M NaOH. The color of the resulting solution turned from transparent to deep black, indicating the formation of Fe-ZnNPs [35]. Then, silica gel 60 was mixed with Fe-ZnNPs using a simple impregnation method [36]. 0.5 grams of silica gel 60 were introduced into the bimetallic nanoparticles solution and the mixture was agitated for three hours at 25°C. The resulting composite material (Si/Fe-ZnNPs) was separated through centrifugation washed with deionized water and dried in an oven at 105°C over 12 hours.

2.3. Characterization studies

Functional groups of Si/Fe-ZnNPs were identified using Perkin Elmer model Fourier Transform Infrared (FT-IR) spectrometer in the range of 4000–400 cm^{-1} using a resolution of 4 cm^{-1} and 32 scans. The crystal phase was determined using X-ray powder diffraction (XRD) analysis using nickel-filtered Cu Kα radiation in a Philips XPert MPD apparatus operated at 40 kV and 30 mA, in the 2θ range of 10°–90°. The morphology was determined through Scanning Electron Microscope (SEM) analysis utilizing the Zeiss/Supra 55 SEM apparatus. The mean diameter of the Fe-Zn bimetallic nanoparticles was determined through Image J software. The recognition of elements and quantitative analysis of composite materials was carried out using the Energy Dispersive X-ray (EDX) technique using the Zeiss/Supra 55 EDX device. The pH at the point of zero charge (pH_{pzc}) of Si/Fe-ZnNPs was obtained by measuring the ζ (zeta) potential at different ranges of pH (2.0–7.0) with Zetasizer (Malvern Zetasizer Nano ZS model). The pH values of the Si/Fe-ZnNPs suspensions were adjusted from 2.0 to 7.0 by adding 0.1 M HCl or 0.1 M NaOH solutions as required.

2.4. Adsorption studies

The adsorption experiments were conducted using a shaking water bath (Memmert WB 29 model) and 250 mL Erlenmayers with a volume of 100 mL of MG dye solution. MG solutions were prepared with a known initial dye concentration at the natural pH (≈ 3.3) of MG.

Samples were taken before the addition of adsorbent for measuring initial MG dye concentrations. Afterward, 0.1 g of adsorbent, except for adsorbent concentration experiments, was contacted with 100 mL of dye solution at the known initial dye concentration and natural pH of MG. Then, the flasks were agitated at a constant temperature and shaking rate for 180 min which is more than ample time for adsorption equilibrium. Samples (3 mL) were withdrawn from the adsorption solution at pre-determined time intervals (2, 5, 10, 15, 30, 45, 60, 90, 120, and 180 min) and subjected to centrifugation at 3500 rpm for 5 min. The resultant supernatant was analyzed using a UV-vis spectrophotometer (Specord 210 Plus, Analytic Jena, Germany) with a wavelength of 618 nm employed to measure the concentration of unadsorbed dye present within the solution.

According to the difference between the initial and residual concentration of MG solution before and after adsorption, the adsorption capacity at time t [q_t; (mg/g)], equilibrium adsorption capacity [q_e; (mg/g)], and the percentage of adsorption [Adsorption (%)] at equilibrium were calculated with Equations (1 – 3).

$$q_t\ (mg/g) = \frac{C_0 - C_t}{m} \cdot V \quad (1)$$

$$q_e\ (mg/g) = \frac{C_0 - C_e}{m} \cdot V \quad (2)$$

$$\text{Adsorption}\ (\%) = \left[\frac{(C_0 - C_e)}{C_0}\right] \cdot 100 \quad (3)$$

Where C_o, C_t, and C_e represent the initial, time t, and equilibrium concentrations of MG solution, respectively, in units of mg/L. Additionally, m denotes the mass of the adsorbent in grams and V is the volume of the liquid phase in liters.

Experiments were carried out with different initial MG dye concentrations (100–500 mg/L), adsorbent concentrations (0.5–3 g/L), and temperatures (25–50°C) values at the natural pH (≈ 3.3) of MG solutions to determine the optimum adsorption conditions. The MG dye solutions ranging from 100–500 mg/L were prepared by diluting the 1.0 g/L stock solution of MG.

3. Results and Discussion

3.1. Characterization of composite material

3.1.1. SEM analysis

The morphology of Si/Fe ZnNPs was characterized by SEM analysis. In Figure 2 (a, b) and (c, d) the SEM images of the Si/Fe ZnNPs before and after adsorption are shown at different magnifications.

The SEM images (Figure 2 (a, b)) demonstrated that the agglomerated spherical nanosized (≈30 nm) particles and the cubic structures were formed. After MG adsorption, as shown in Figure 2 (c, d), it was observed that the morphological structure changed, the spherical nanoparticles were more agglomerated and the structures in the cubic forms disappeared.

3.1.2. EDX analysis

The EDX spectra before and after adsorption are shown in Figure 3 (a), and (b), and the elemental and quantitative weight composition (wt%) of Si/Fe-ZnNPs is shown in the inset of Figure 3 (a).

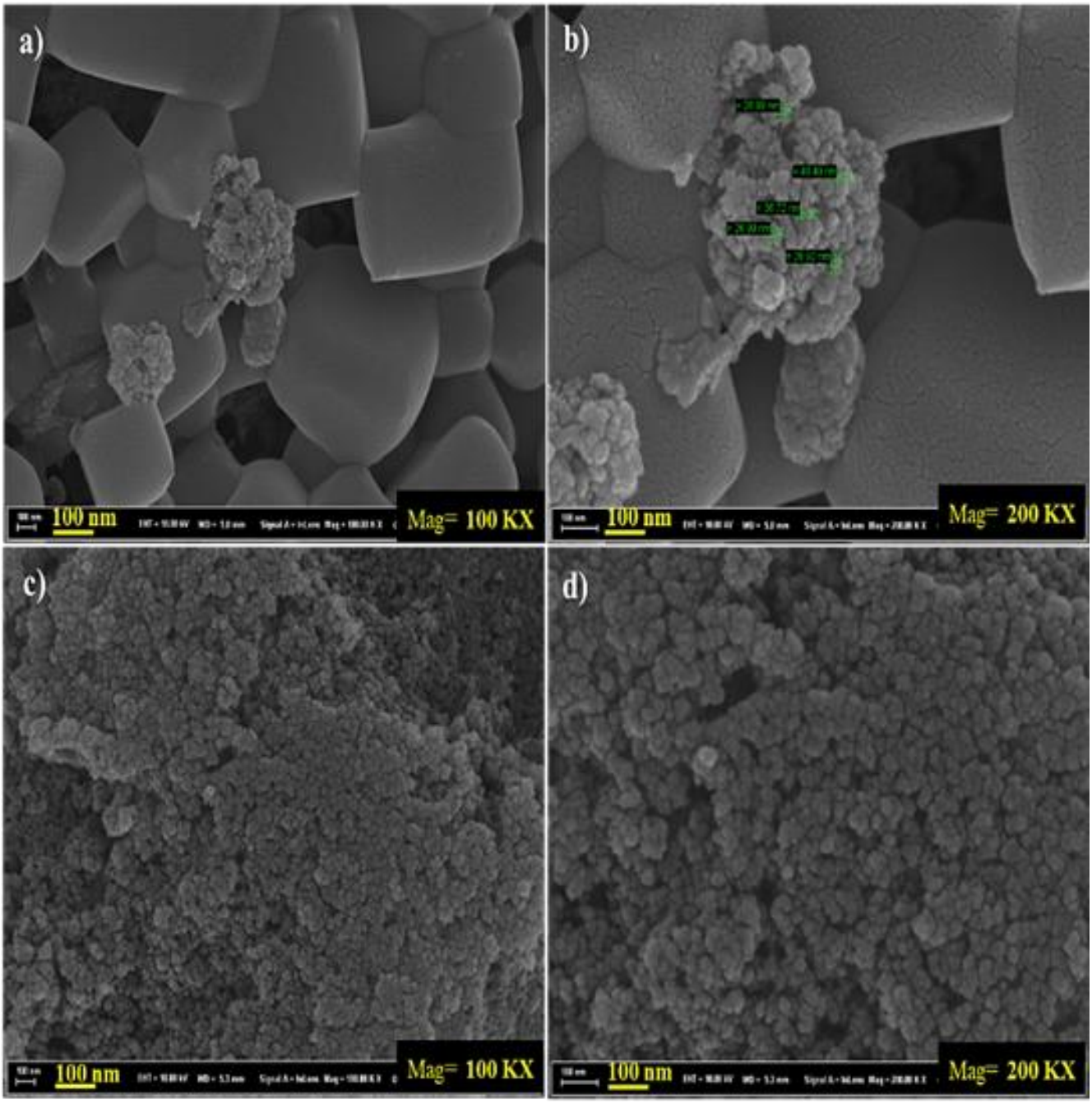

Figure 2. SEM images of Si/Fe-ZnNPs a) – 100 nm, 100 KX, b) – 100 nm, 200 KX before adsorption, c) – 100 nm, 100 KX, d) – 100 nm, 200 KX; after adsorption.

According to EDX analysis results, the weight composition (wt%) of Si/Fe-ZnNPs was determined as 6.78% Fe, 44.07% Zn, 2.44%Si, 8.56% O, and 38.14% Cl. It is worth mentioning that the data are the points on the adsorbent surface and are not the average content [37]. The formation of Si/Fe-ZnNPs was approved by the signals in Fe, Zn, O, and Si regions. Furthermore, following the adsorption (Figure 3(b)), the signals of C and N elements were also detected. This result confirmed that the dye molecules were adsorbed onto the surface of the adsorbent.

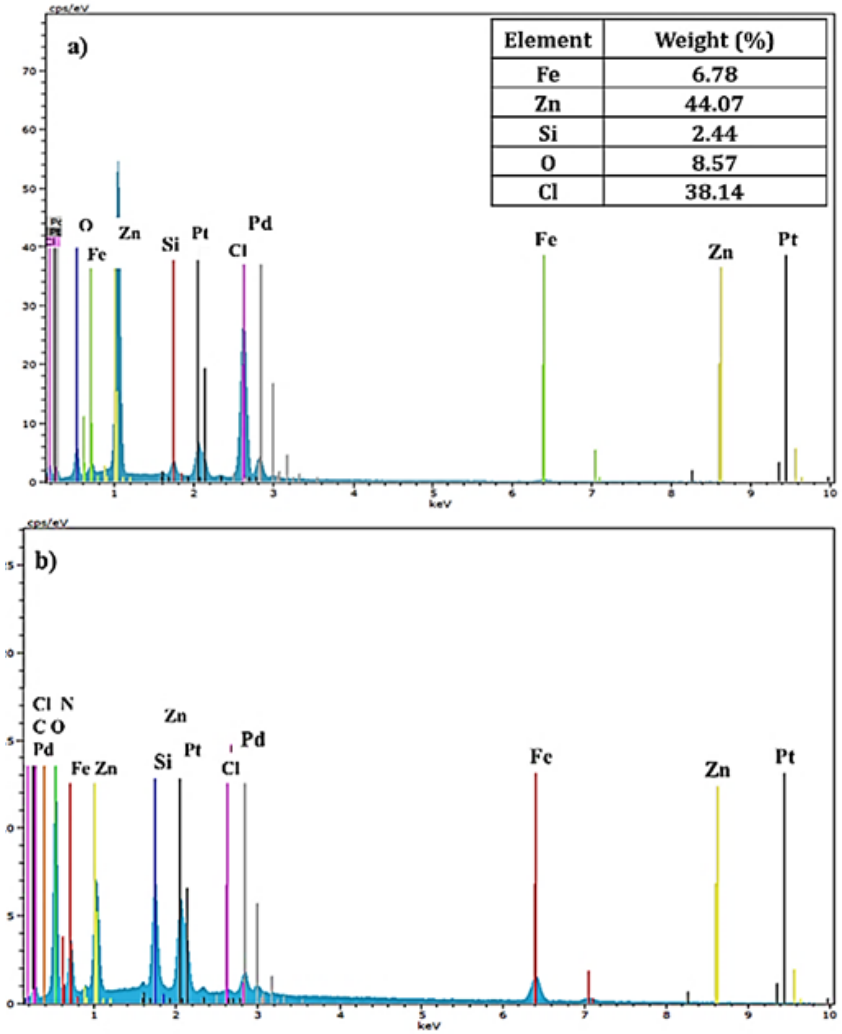

Figure 3. EDX spectra of composite material a) before adsorption and b) after adsorption.

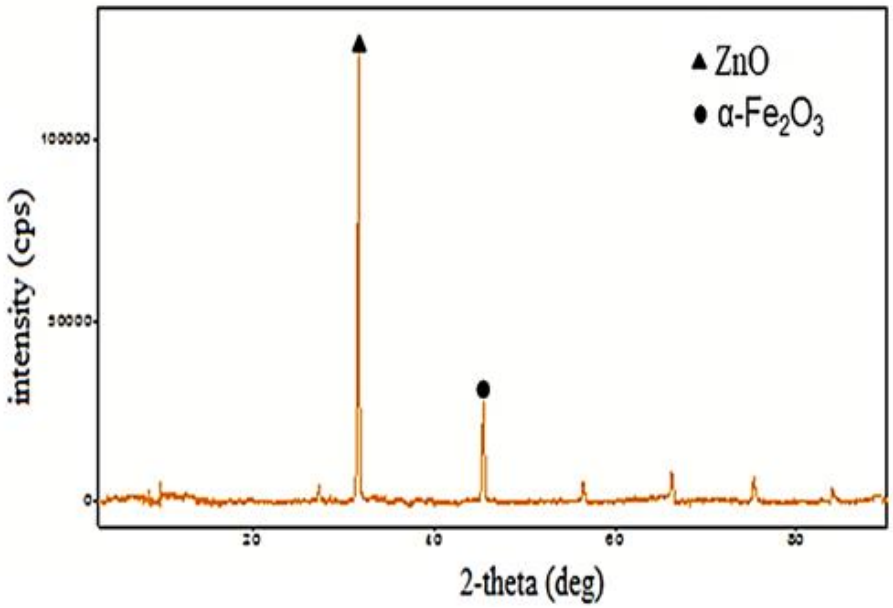

Figure 4. XRD pattern of synthesized Si/Fe-ZnNPs.

3.1.3. XRD analysis

The XRD pattern of synthesized Si/Fe-ZnNPs is given in Figure 4.

The peaks at 2θ = 34° and 45° correspond to the structures of ZnO and maghemite (α-Fe_2O_3), respectively Also, the weak peaks at 56°, and 66° corresponded to zinc oxide [38, 39]. The characteristic diffuse peak of silica is about 2θ = 21.6°. However, the characteristic peak of silica gel was not obtained in the XRD pattern.

This could demonstrate that a high percentage of structure is amorphous [40]. Moreover, this may be due to the low content and relatively low diffraction intensity of SiO_2 [41]. After adsorption, the XRD diagram showed that the material was completely amorphous. This was due to the change in crystallinity and phase.

3.1.4. FT-IR analysis

The FT-IR spectra of the Si/Fe-ZnNPs pre and post-adsorption can be seen in Figure 5, while feasible assignments are found in Table 1. The FT-IR spectra of Si/Fe-ZnNPs before and after adsorption did not show any significant changes as shown in Figure 5. Accordingly, the bands at 3650 cm^{-1}, 1618 cm^{-1}, and 954 cm^{-1} corresponded to O-H stretching vibration related to hydrogen bond, strain of υ(C-N) bond, and C – O stretching vibration, respectively. Furthermore, the absorption peaks at 522 cm^{-1} and 467 cm^{-1} correspond to Fe-O stretches of α-Fe_2O_3 and metal-metal stretching vibrations of (Zn^{2+} – O^{2-}) in the tetrahedral region, respectively, suggesting the formation of Fe-ZnNPs. At the absorption bands of 1067.8 cm^{-1} and 490.96 cm^{-1}, Si-O-H, Si-O-Si stretching, and O-Si-O bending vibrations were detected [42–45].

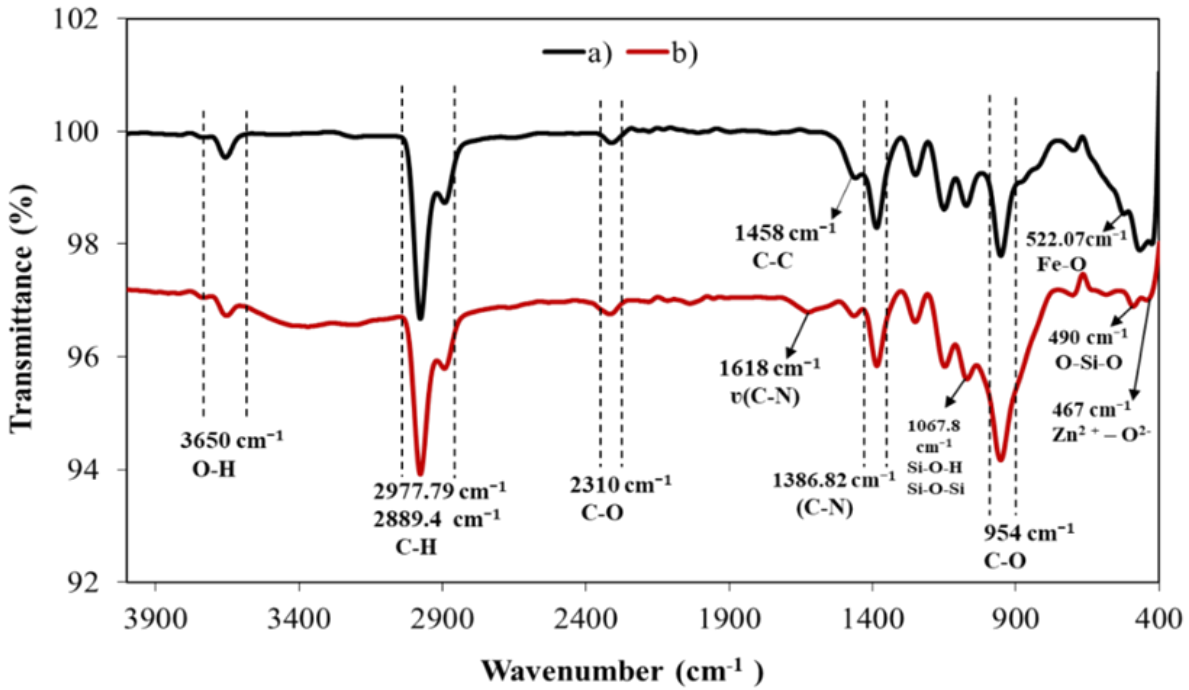

Figure 5. FT-IR spectrum of Si/Fe ZnNPs a) before b) after adsorption.

Table 1. FTIR spectra with suggested assignments.

Frequency (cm^{-1})	Assignment
3650	O-H stretching vibration related to hydrogen bond
2977.79	C-H stretching vibration
2889.4	C-H stretching vibration
2310.1	C-O bending
1618	Strain of υ(C-N) bond
1458	C–C stretching vibration
1386.82	Aromatic amine (C-N) stretching
1067.8	Si-O-H and Si-O-Si stretching vibrations
954	C – O stretching vibration
522	Fe-O stretches of α-Fe_2O_3
490.96	O-Si-O bending vibration
467	Metal-metal stretching vibration of (Zn^{2+} – O^{2-}) in tetrahedral region

3.1.5. Determination of pH of zero point of charge (pH_{zpc})

The isoelectric point (point of zero charge ((pH_{pzc})) of Si/Fe-ZnNPs was determined by zeta potential measurement at different pH (2.0 – 7.0) values and the change of the zeta potential with pH is presented in Figure 6.

The point of zero charge (pH_{pzc}) of Si/Fe-ZnNPs was determined to be 4.30, as shown in Figure 6. The point of

zero charge (pH_{pzc}) is the pH of the solution where the charge of the positive surface sites equals that of the negative sites, meaning the adsorbent surface charge is zero. The surface charge is negative at $pH>pH_{pzc}$ and positive at $pH<pH_{pzc}$ [46].

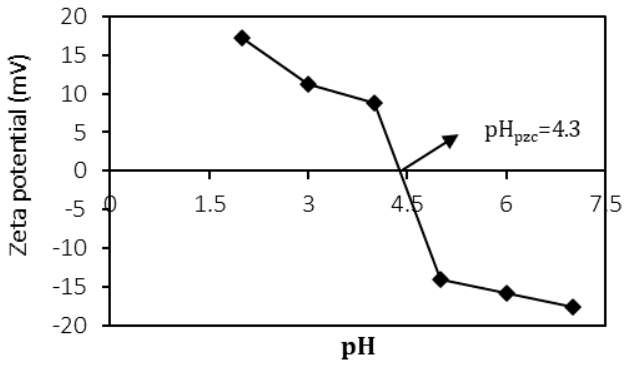

Figure 6. The isoelectric point of Si/Fe-ZnNPs.

3.2. Influence of environmental conditions

The effect of process parameters on adsorption was examined in a batch system, considering the initial pH of the solution, initial dye concentration, adsorbent concentration, and temperature. The results are presented in the following sub-sections.

3.2.1. Influence of initial pH

The initial pH of the solution is an important factor that affects the adsorption. The initial pH of the solution can alter the surface charge of the adsorbent, the degree to which the contaminants are ionized, and the structure of the dye molecules [47].

The determination of the point of zero charge (pH_{pzc}) of the adsorbent is necessary to gain a better understanding of the pH effect. The pH_{pzc} of Si/Fe-ZnNPs was determined to be 4.30, as indicated in Figure 6. This indicates that when adsorption occurs at pH values above the pH_{pzc} of the adsorbent, the surface of the adsorbent becomes negatively charged and the adsorption capacity increases due to the strong electrostatic attraction between the negatively charged surface of the adsorbent and the cationic dye. However, no pH adjustment was made in this study since; it was observed that dyestuff molecules collapsed when the adsorbent-free solutions of MG were adjusted to basic pH values over the pH_{pzc} of the adsorbent. The attitude of obtaining high adsorption capacity at a natural pH of 3.3, can be explained by the natural pH of the solution being near the pH_{pzc} of the adsorbent.

3.2.2. Influence of initial dye concentration

The influence of initial dye concentration on adsorption was investigated within the range of 100 – 500 mg/L MG dye concentration.

The initial dye concentration effect on adsorption is illustrated in Figure 7.

As seen from Figure 7, the equilibrium adsorption capacities increased linearly ($q_e=0.9745*C_o$, $R^2=0.999$) in the studied dye concentrations as a result of the increase in the driving force (ΔC) to get over mass transfer resistances of the dye molecules between the aqueous and solid phases [48]. Moreover, obtaining high equilibrium uptakes allows working in the wide dyestuff concentration ranges.

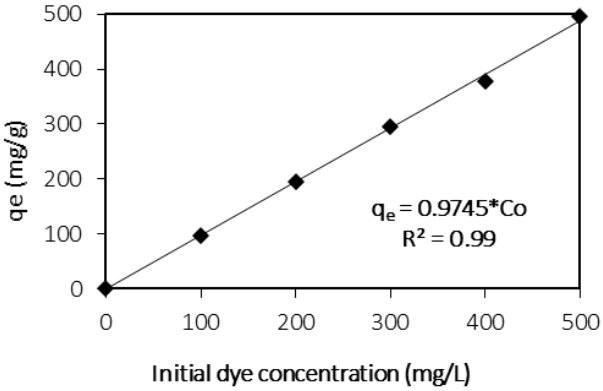

Figure 7. The effect of initial dye concentration (initial pH= natural pH≈ 3.3, X_0 =1 g/L, T= 50°C, t=180 min).

3.2.3. Influence of adsorbent concentration

The effect of adsorbent concentration was investigated in the range of 0.5 – 3.0 g/L adsorbent concentration. The adsorbent concentration effect on the equilibrium adsorption capacity and the percentage of adsorption was demonstrated in Figure 8.

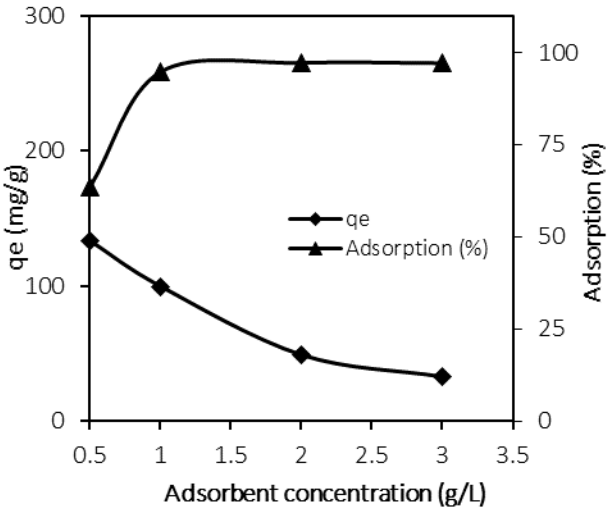

Figure 8. The impact of adsorbent concentration (initial pH= natural pH≈ 3.3, C_0 =100 mg/L, T=50°C, t=180 min).

Figure 8 illustrates the equilibrium adsorption capacities and adsorption percentages obtained for the adsorbent concentrations in the range from 0.5 g/L to 3 g/L. According to Figure 8, the equilibrium adsorption capacities decreased as the concentration of the adsorbents increased from 0.5 g/L to 3 g/L. Nevertheless, there was a marked increase in the adsorption percentage up to an adsorbent concentration of 1.0 g/L, which then became relatively constant with a further increase in adsorbent concentration. The decline in adsorption capacities as the adsorbent concentration increases could result from the agglomeration of

adsorbent particles caused by high adsorbent concentration. The agglomeration can cause a reduction in the active surface area of the adsorbent and an increase in the length of the diffusional pathway [48]. Thus, the reason for achieving lower adsorption capacities at 2 g/L and 3 g/L of adsorbent concentrations could be agglomeration. As a consequence of the experiment, the optimum adsorbent concentration was determined to be 1.0 g/L for the MG adsorption.

3.2.4. Influence of temperature

The effect of temperature was studied at three different values: 25°C, 35°C and 50°C values. The impact of the temperature is shown in Figure 9 below.

Figure 9 illustrates that a higher adsorption capacity was achieved with a temperature increase from 25°C to 50°C leading to the determination of the optimum temperature for MG adsorption as 50°C. The results indicate that the studied adsorption process is endothermic, given the high operation temperature.

The influence of environmental conditions such as initial pH, initial dye concentration, adsorbent concentration, time, and reaction temperature are summarized in Table 2. It presents a summary of the various adsorbents documented in scientific papers for the adsorption of MG. From Table 2, we can see that the value obtained in our study is significantly higher than the adsorption capacity observed in studies using silica gel and Fe-ZnNPs separately as adsorbents for MG removal.

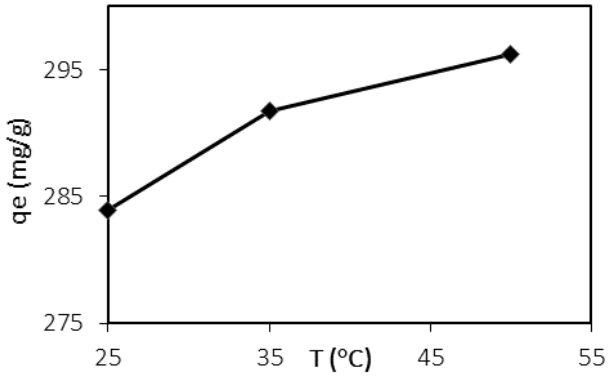

Figure 9. The effect of temperature (initial pH= natural pH≈ 3.3, C_0 =300 mg/L, X_0 =1 g/L, t=180 min).

Table 2. Effect of adsorption parameters of various adsorbents for MG removal in the literature.

Adsorbent	Initial pH	Initial Dye Conc. (mg/L)	Adsorbent Conc. (g/L)	Time (min)	Temp. (°C)	Adsorption Capacity (mg/g)	Removal Eff. (%)	Reference
Acid-functionalized silica nanoparticles	6.5	10	2.0	60	22	116.3	–	[33]
Mesoporous magnetic corn straw-derived biochar supported nZVI composite	6.0	100	0.25	20	25	515.77	99.9	[50]
Cellulose nanofibers and silver nanoparticles composites	8.0	100	0.5	100	30	142	78	[51]
Polymer hybrid bio-nanocomposite	7.0	150	1.0	40	50	384.615	99.79	[52]
GO@ZnO-$NiFe_2O_4$-αAl_2O_3 nanocomposites	7.0	1500	2.0	90	25	607.66	82	[53]
Calcium silicate nanopowders from waste materials	6.5	10	0.7	60	30	59.95	100	[54]
Multi-walled Carbon nanotube modified with Carboxylate group MWCNT-COOH	9.0	50	1.0	10	55	11.73	91.36	[55]
SDS/CTAB@Mt composite	7.0	1200	1.0	140	25	1021.45	99.32	[56]
Carbon dots/silica nano aggregates	6.0	200	0.05	2880	35	4091	–	[57]
Silica gel 60	2.3	29.2	3.5	1200	35	39.7	–	[31]
Fe-ZnNPs	9.0	25	3.0	60	30	28.56	92	[11]
Si/Fe-ZnNPs	No pH adjustment	100	1.0	180	50	666.67	96.81	This work

3.2.5. Thermodynamic studies

The effect of temperature was confirmed through thermodynamic parameters, including the change in Gibbs' free energy (ΔG), the change in enthalpy (ΔH), and the change in entropy (ΔS), which were calculated using the Van't Hoff equation. The Equations 4-5 were employed to determine ΔG, ΔH, and ΔS [49].

ΔH and ΔS were obtained by determining the slope and intercept of the linear plot of ln K_c against 1/T, by

Van't Hoff Equation 4. Furthermore, ΔG was computed following Equation 5.

The equilibrium constant (K_c) values were calculated utilizing Equation 6.

$$\ln K_c = \left(\frac{\Delta S}{R}\right) - \left(\frac{\Delta H}{R}\right) \cdot \frac{1}{T} \quad (4)$$

$$\Delta G = -RT \ln Kc = \Delta H - T\Delta S \quad (5)$$

$$K_c = \frac{C_{ad,e}}{C_e} \quad (6)$$

Where $C_{ad,e}$, and C_e represent the equilibrium concentrations (mg/L) of adsorbed and unadsorbed dyestuff ions, respectively. $C_{ad,e}$ is equal to q_e at the studied temperature when the adsorbent concentration is 1.0 g/L. In this study, we found the linear form of the Van't Hoff equation for adsorption to be $\ln K_c$ = -2348.9*1/T + 3.8537, with a regression coefficient of 0.999 (data not shown). Additionally, the calculated corresponding thermodynamic parameters are presented in Table 3.

As seen from Table 3, the positive ΔH value indicated the adsorption system was endothermic. The positive ΔG values showed that adsorption was non-spontaneous. Furthermore, a decrease in ΔG values with an increase in temperature showed that adsorption was more favorable at higher temperatures. The positive ΔS value reflected the irreversibility of adsorption and the randomness of the dye species adsorbed at the solid/solution interface.

Table 3. Thermodynamic parameters of adsorption.

T(K)	ΔG (J/mole)	ΔH (kJ/mole)	ΔS (J/mole.K)
298	9968.582		
308	9681.758	19.530	32.039
323	9170.201		

3.3. Modelling studies

3.3.1. Modelling adsorption equilibrium

The experimental equilibrium data for MG adsorption at the investigated temperatures were fitted with the renowned linearized forms of the Langmuir and Freundlich isotherm models.

The Langmuir isotherm presumes that the species adsorbed are in equilibrium with the adsorbent. The model relies on primary presumptions i) Adsorption occurs in a monolayer. ii) No interaction exists between the adsorbed molecules. iii) The surface is homogeneous, with identical binding sites [58].

The Freundlich isotherm model is a modification of the Langmuir isotherm that describes multilayer adsorption on heterogeneous surfaces [59].

The linearized forms of models are given in Equation 7:

$$\text{Langmuir: } \frac{1}{q_e} = \frac{1}{Q^\circ b} \cdot \frac{1}{C_e} + \frac{1}{Q^\circ} \quad (7)$$

$$\text{Freundlich: } \ln q_e = \ln K_F + \left(\frac{1}{n}\right) \ln C_e \quad (8)$$

where:

q_e is the adsorbed amount per unit mass of adsorbent (mg/g);

C_e is the unadsorbed dyestuff concentration at equilibrium (mg/L);

Q^o is the maximum monolayer coverage capacity of adsorbent (mg/g);

b is a Langmuir constant associated with binding site affinity (L/mg);

K_F is the adsorption capacity indicated by the Freundlich constant ((mg/g)/(L/mg)$^{1/n}$);

1/n is the Freundlich constant indicative of adsorption intensity.

The isothermal constants and their corresponding regression coefficients (R^2) were presented in Table 4 and the comparison of experimental and modeled isotherms at 50°C was given in Figure 10. Table 4 and Figure 10 demonstrate that the Langmuir isotherm model is in good agreement with the experimental equilibrium data, as indicated by the higher regression coefficients. The results show that a monolayer coating of MG was formed on the surface of Si/Fe-ZnNPs, indicating that the process took place at specific homogeneous sites within the adsorbent.

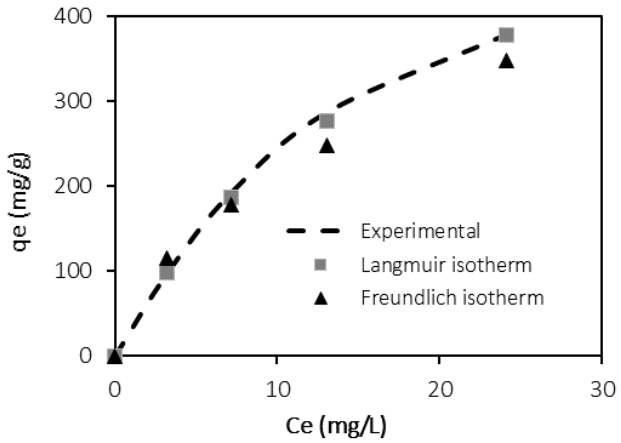

Figure 10. The comparison of the experimental and the predicted isotherms.

The maximum monolayer coverage capacity (Q°) of the adsorbent was determined to be 666.67 mg/g at 50 °C, which is the optimum temperature. As shown in Table 4, the maximum monolayer coverage capacity values of the adsorbent for MG increased with increasing temperature because of the adsorption process is endothermic. The maximum adsorption capacity (Q°) of Si/Fe ZnNPs was contrasted with that of Q° values of different adsorbents reported for MG adsorption. The comparison of Q° values is given in Table 5. Table 5 shows that the adsorption capacity of Si/Fe-ZnNPs was good when compared with other studies.

3.3.2. Kinetic modelling

Adsorption kinetics were explained by correlating adsorption kinetic data using linear forms of Lagergen's pseudo-first-order (PFO) [71] and pseudo-second order kinetic (PSO) models [72]. Equations 9 and 10 give the linearized forms of models:

Table 4. The constants of the isotherm models with the values of the regression coefficient (R^2).

T (°C)	Langmuir isotherm model [$q_e = Q^o b C_e / (1+bC_e)$]			Freundlich isotherm model [$q_e = K_F C_e^{1/n}$]		
	Q^o	b	R^2	K_F	1/n	R^2
25	476.19	0.1468	0.999	60.327	0.549	0.942
35	625.00	0.0994	0.999	80.356	0.544	0.944
50	666.67	0.05395	0.998	98.612	0.373	0.909

Table 5. Maximum adsorption capacity (Q°) of Si/Fe-ZnNPs with other reported adsorbents in the literature for MG dye adsorption.

Adsorbent	Langmuir isotherm model Q°(mg/g)	References
Modified rice husk	996.97	[60]
Fe_3O_4/β-CD/GO	740.74	[61]
nZVI magnetic composite supported by straw biochar (nZVI/BC)	515.77	[50]
Magnetic $CuFe_2O_4$ nano-adsorbent	197	[62]
ZnS: Cu nanoparticle-loaded activated carbon	168.1	[63]
Graphene oxide/aminated lignin aerogels	113.5	[64]
Natural zeolite	98.04	[65]
Rattan sawdust	62.71	[66]
Multi-walled carbon nanotubes functionalized with carboxylates	49.45	[67]
Sodium alginate-coated superparamagnetic Fe_3O_4 nanoparticles	47.84	[68]
Montmorillonite/PVDF/PEO microporous membranes	33.4	[69]
Zeolite synthesized using silica gel (ZS)	29.744	[25]
ZnO nanorod-loaded activated carbon	20	[70]
(Si/Fe-Zn NPs)	666.67	This study

$$\text{PFO: } \log(q_e - q_t) = \log(q_e) - \frac{k_1 t}{2.303} \quad (9)$$

$$\text{PSO: } \frac{t}{q_t} = \left(\frac{1}{q_e^2 k_2}\right) + \frac{t}{q_e} \quad (10)$$

where:

q_e is the adsorbed amount per unit mass of adsorbent (mg/g);

q_t is the adsorbed amount per unit mass of adsorbent at any time (mg/g);

k_1 is the pseudo-first-order kinetic rate constant (1/min);

k_2 is the sseudo-second-order kinetic rate constant (g/mg.min)

The parameters with regression coefficients of the PFO and PSO kinetic models are shown in Table 6.

The nomenclatures shown in Table 6 are as follows:

$q_{e,exp}$ is the experimental adsorbed amount per unit mass of adsorbent (mg/g);

q_{e,cal_1} is the calculated amount of adsorbed substance per unit mass of adsorbent from the pseudo-first-order kinetic model (mg/g);

q_{e,cal_2} is the calculated amount of adsorbed substance per unit mass of adsorbent from the pseudo-second-order kinetic model (mg/g).

From Table 6, an excellent fit of the PSO kinetics was shown by the higher R^2 values and the agreement between experimental and calculated equilibrium adsorption capacities. If the adsorption data conforms to the PSO kinetic model, chemisorption via electron exchange or sharing between functional groups on the sorbent and dyestuff ions predominantly occurs [72].

Table 6. Model parameters with R^2 values for kinetics and mass transfer.

C_o (mg/L)	$q_{e,exp}$ (mg/g)	PFO			PSO			Weber-Morris Model		
		k_1 (min^{-1})	q_{e,cal_1} (mg/g)	R^2	k_2 (g/mg.min)	q_{e,cal_2} (mg/g)	R^2	K_i ($mg/g.min^{0.5}$)	Intercept	R^2
100.96	97.75	0.0304	10.73	0.649	0.01553	97.75	0.999	0.1593	95.778	0.999
199.89	194.49	0.0278	24.67	0.575	0.01000	193.95	0.999	0.2026	189.95	0.998
300.53	292.75	0.0232	53.80	0.725	0.00031	275.99	0.999	4.7475	253.06	0.997
402.57	378.43	0.0315	138.36	0.913	0.00111	373.48	0.999	13.096	272.14	0.997
509.00	496.21	0.0039	361.83	0.910	0.00023	379.11	0.994	14.400	323.75	0.996

3.3.3. Mass transfer modelling

The Weber-Morris model was used to examine the interfacial layer and intraparticle diffusion mechanism between dye and adsorbent, and the model parameters and regression coefficients were summarized in Table 6. The Weber-Morris model is defined by Equation (11) [73].

$$q_t = K_i . t^{0.5} + I \quad (11)$$

In the Weber-Morris equation, I is the cut-off point associated with the interfacial effect, and Ki is the rate constant of intra-particle diffusion ((mg/g.min1/2)). The Ki value can be obtained by determining the slope of the linear graph of qt versus t0.5. This model suggests that if a linear plot of qe versus t0.5 lies through the origin, it suggests that intra-particle diffusion is the only rate-controlling step. Nevertheless, the line may not always cross the origin, as the diffusion kinetics of adsorption can be controlled simultaneously by film diffusion and pore diffusion. In this case, multilinear plots can be

obtained with an intercept value. Based on the results, a multilinear plot was observed in this study. This suggests that pore and film diffusion play a role in the adsorption process.

4. Conclusion

A composite material of Si/Fe-ZnNPs was synthesized and subsequently used in this study for MG adsorption. The material was characterized by means of SEM, EDX, FTIR, and XRD analyses. Adsorption studies were performed to determine the influence of operating parameters over the adsorption of MG. The study revealed that an adsorption percentage of 96.81% was obtained in 180 minutes, utilizing natural pH of solution (≈ 3.3), an adsorbent concentration of 1.0 g/L, and a temperature of 50°C with a 100 mg/L of MG. The Langmuir isotherm model was employed to model the adsorption equilibrium. This model assumes of monolayer adsorption on a homogeneous surface. According to the thermodynamic parameters, positive values of ΔG, ΔH, and ΔS indicate that the process was non-spontaneous and endothermic and that the disorder at the solid/solution interface increased during the process. The kinetic data are consistent with the PSO kinetic model, and mass transfer modeling studies showed that both intraparticle and film diffusion appear to be effective.

Consequently, the research findings demonstrate that the Si/Fe-ZnNPs composite material synthesized is an effective adsorbent for eliminating MG dye from aqueous solutions.

Author contributions

Memduha Ergüt: Conceptualization, Methodology, Validation, Formal analysis, Data curation, Writing – original draft, Visualization. **Ayla Özer:** Review & editing, Supervision, Funding acquisition

Conflicts of interest

The authors declare no conflicts of interest.

References

1. Rathi, B. S., & Kumar, P. S. (2021). Application of adsorption process for effective removal of emerging contaminants from water and wastewater. Environmental pollution (Barking, Essex: 1987), 280, 116995. https://doi.org/10.1016/j.envpol.2021.116995
2. Ahmad, H. R., Aziz, T., Zia-ur-Rehman, M., Sabir, M., & Khalid, H. (2016). Sources and composition of waste water: Threats to plants and soil health. In Soil Science: Agricultural and Environmental Prospectives (349–370). Springer International Publishing. https://doi.org/10.1007/978-3-319-34451-5_16
3. Senthil Kumar, P., Joshiba, G. J., Femina, C. C., Varshini, P., Priyadharshini, S., Arun Karthick, M. S., & Jothirani, R. (2019). A critical review on recent developments in the low-cost adsorption of dyes from wastewater. Desalination And Water Treatment, 172, 395–416. https://doi.org/10.5004/dwt.2019.24613
4. Ahmouda, K., Boudiaf, M., & Benhaoua, B. (2022). A novel study on the preferential attachment of chromophore and auxochrome groups in azo dye adsorption on different greenly synthesized magnetite nanoparticles: investigation of the influence of the mediating plant extract's acidity. Nanoscale Advances, 4(15),3250–3271. https://doi.org/10.1039/d2na00302c
5. Oruç, Z., Ergüt, M., Uzunoğlu, D., & Özer, A. (2019). Green synthesis of biomass-derived activated carbon/Fe-Zn bimetallic nanoparticles from lemon (Citrus limon (L.) Burm. f.) wastes for heterogeneous Fenton-like decolorization of Reactive Red 2. Journal of Environmental Chemical Engineering, 7(4), 103231. https://doi.org/10.1016/j.jece.2019.103231
6. Swan, N. B., & Zaini, M. A. A. (2019). Adsorption of Malachite Green and Congo Red Dyes from Water: Recent Progress and Future Outlook. Ecological Chemistry and Engineering S, 26(1), 119–132. https://doi.org/10.1515/eces-2019-0009
7. M. Nahiun, K., Sarker, B., N. Keya, K., I. Mahir, F., Shahida, S., & A. Khan, R. (2021). A Review on the Methods of Industrial Waste Water Treatment. Scientific Review, 7(73), 20–31. https://doi.org/10.32861/sr.73.20.31
8. Tulun, Ş., Bahadir, T., Şimşek, İ., & Karataş, M. (2019). The removal of nickel ions with walnut shell. Turkish Journal of Engineering, 3(2), 102-105. https://doi.org/10.31127/tuje.456741.
9. Sharma, G., Kumar, A., Sharma, S., Naushad, M., Prakash Dwivedi, R., ALOthman, Z. A., & Mola, G. T. (2019). Novel development of nanoparticles to bimetallic nanoparticles and their composites: A review. Journal of King Saud University - Science, 31(2), 257–269. https://doi.org/10.1016/j.jksus.2017.06.012
10. Scaria, J., Nidheesh, P. V, & Kumar, M. S. (2020). Synthesis and applications of various bimetallic nanomaterials in water and wastewater treatment. Journal of Environmental Management, 259,110011. https://doi.org/10.1016/j.jenvman.2019.110011
11. Gautam, R. K., Rawat, V., Banerjee, S., Sanroman, M. A., Soni, S., Singh, S. K., & Chattopadhyaya, M. C. (2015). Synthesis of bimetallic Fe-Zn nanoparticles and its application towards adsorptive removal of carcinogenic dye malachite green and Congo red in water. Journal of Molecular Liquids, 212, 227–236. https://doi.org/10.1016/j.molliq.2015.09.006
12. Kharissova, O. V, Dias, R., & Kharisov, B. I. (2015). Magnetic adsorbents on the basis of micro- and nanostructurized materials. RSC Advances, 5, 6695–6719.
13. Chen, Z. X., Cheng, Y., Chen, Z., Megharaj, M., & Naidu, R. (2014). Kaolin-supported nanoscale zero-valent iron for removing cationic dye–crystal violet in aqueous solution. In Nanotechnology for Sustainable Development, First Edition, 189–196. https://doi.org/10.1007/978-3-319-05041-6_15

14. Hamdy, A., Mostafa, M. K., & Nasr, M. (2018). Zero-valent iron nanoparticles for methylene blue removal from aqueous solutions and textile wastewater treatment, with cost estimation. Water Science and Technology, 78(2), 367–378. https://doi.org/10.2166/wst.2018.306
15. Sahu, N., Rawat, S., Singh, J., Karri, R. R., Lee, S., Choi, J.-S., & Koduru, J. R. (2019). Process Optimization and Modeling of Methylene Blue Adsorption Using Zero-Valent Iron Nanoparticles Synthesized from Sweet Lime Pulp. Applied Sciences, 9(23), 5112. https://doi.org/10.3390/app9235112
16. Naser, R., & Shahwan, T. (2019). Comparative assessment of the decolorization of aqueous bromophenol blue using Fe nanoparticles and Fe-Ni bimetallic nanoparticles. Desalination and Water Treatment, 159, 346-355. https://doi.org/10.5004/dwt.2019.24136
17. Alruqi, S. S., AL-Thabaiti, S. A., & Khan, Z. (2019). Iron-nickel bimetallic nanoparticles: Surfactant assisted synthesis and their catalytic activities. Journal of Molecular Liquids, 282, 448–455. https://doi.org/10.1016/j.molliq.2019.03.021
18. Bokare, A. D., Chikate, R. C., Rode, C. V., & Paknikar, K. M. (2008). Iron-nickel bimetallic nanoparticles for reductive degradation of azo dye Orange G in aqueous solution. Applied Catalysis B: Environmental, 79(3), 270–278. https://doi.org/10.1016/j.apcatb.2007.10.033
19. Tahir, H., Saad, M., Attala, O. A., El-Saoud, W. A., Attia, K. A., Jabeen, S., & Zeb, J. (2023). Sustainable Synthesis of Iron–Zinc Nanocomposites by Azadirachta indica Leaves Extract for RSM-Optimized Sono-Adsorptive Removal of Crystal Violet Dye. Materials, 16(3), 1023. https://doi.org/10.3390/ma16031023
20. Ulucan-Altuntas, K., & Kuzu, S. L. (2019). Modelling and optimization of dye removal by Fe/Cu bimetallic nanoparticles coated with different Cu ratios. Materials Research Express, 6(11), 1150a4. https://doi.org/10.1088/2053-1591/ab4bb5
21. Mahmoud, A. S., Mostafa, M. K., & Peters, R. W. (2021). A prototype of textile wastewater treatment using coagulation and adsorption by Fe/Cu nanoparticles: Techno-economic and scaling-up studies. Nanomaterials and Nanotechnology, 11, 18479804211041181.https://doi.org/10.1177/18479804211041181
22. Raman, C. D., & Kanmani, S. (2016). Textile dye degradation using nano zero valent iron: A review. Journal of Environmental Management, 177, 341–355. https://doi.org/10.1016/j.jenvman.2016.04.034
23. Bhattacharya, S., Saha, I., Mukhopadhyay, A., Chattopadhyay, D., & Chand, U. (2013). Role of nanotechnology in water treatment and purification: Potential applications and implications. International Journal of Chemical Science and Technology, 3(3), 59–64.
24. Kharisov, B. I., Dias, H. R., Kharissova, O. V., Jiménez-Pérez, V. M., Pérez, B. O., & Flores, B. M. (2012). Iron-containing nanomaterials: synthesis, properties, and environmental applications. Rsc Advances, 2(25), 9325-9358.
25. Abdelrahman, E. A. (2018). Synthesis of zeolite nanostructures from waste aluminum cans for efficient removal of malachite green dye from aqueous media. Journal of Molecular Liquids, 253, 72–82. https://doi.org/10.1016/j.molliq.2018.01.038
26. Maher, H., Rupam, T. H., Rocky, K. A., Bassiouny, R., & Saha, B. B. (2022). Silica gel-MIL 100(Fe) composite adsorbents for ultra-low heat-driven atmospheric water harvester. Energy, 238, 121741. https://doi.org/10.1016/j.energy.2021.121741
27. Boukoussa, B., Mokhtar, A., El Guerdaoui, A., Hachemaoui, M., Ouachtak, H., Abdelkrim, S., Addi Ait, A., Babou, S., Boudina, B., Bengueddach, A., Hamacha, R. (2021). Adsorption behavior of cationic dye on mesoporous silica SBA-15 carried by calcium alginate beads: Experimental and molecular dynamics study. Journal of Molecular Liquids, 333, 115976. https://doi.org/10.1016/j.molliq.2021.115976
28. Volikov, A. B., Ponomarenko, S. A., Konstantinov, A. I., Hatfield, K., & Perminova, I. V. (2016). Nature-like solution for removal of direct brown 1 azo dye from aqueous phase using humics-modified silica gel. Chemosphere, 145, 83–88. https://doi.org/10.1016/j.chemosphere.2015.11.070
29. Patra, A. S., Ghorai, S., Sarkar, D., Das, R., Sarkar, S., & Pal, S. (2017). Anionically functionalized guar gum embedded with silica nanoparticles: An efficient nanocomposite adsorbent for rapid adsorptive removal of toxic cationic dyes and metal ions. Bioresource Technology, 225, 367–376. https://doi.org/10.1016/j.biortech.2016.11.093
30. Zhang, Y., Xia, K., Liu, X., Chen, Z., Du, H., & Zhang, X. (2019). Synthesis of cationic-modified silica gel and its adsorption properties for anionic dyes. Journal of the Taiwan Institute of Chemical Engineers, 102, 1–8. https://doi.org/10.1016/j.jtice.2019.05.005
31. Samiey, B., & Toosi, A. R. (2010). Adsorption of malachite green on silica gel: effects of NaCl, pH and 2-propanol. Journal of hazardous materials, 184(1–3), 739–745. https://doi.org/10.1016/j.jhazmat.2010.08.101
32. Mansa, R. F., Sipaut, C. S., Rahman, I. A., Yusof, N. S. M., & Jafarzadeh, M. (2016). Preparation of glycine–modified silica nanoparticles for the adsorption of malachite green dye. Journal of Porous Materials, 23(1), 35–46. https://doi.org/10.1007/s10934-015-0053-3
33. Hassan-Zadeh, B., Rahmanian, R., Salmani, M. H., & Salmani, M. J. (2021). Functionalization of Synthesized Nanoporous Silica and Its Application in Malachite Green Removal from Contaminated Water. Journal of Environmental Health and Sustainable Development, 6(2), 1311–1320. https://doi.org/10.18502/jehsd.v6i2.6542
34. Hossain, M. A., Hossain, M. L., & Hassan, T. Al. (2016). Equilibrium, Thermodynamic and Mechanism Studies of Malachite Green Adsorption on Used Black Tea Leaves from Acidic Solution. International Letters of Chemistry, Physics and Astronomy, 64(2018), 77–88. https://doi.org/10.56431/p-c20qfs
35. Kaya, M., Zahmakiran, M., Özkar, S., & Volkan, M. (2012). Copper(0) nanoparticles supported on silica-

coated cobalt ferrite magnetic particles: Cost effective catalyst in the hydrolysis of ammonia-borane with an exceptional reusability performance. ACS Applied Materials and Interfaces, 4(8), 3866–3873. https://doi.org/10.1021/am3005994

36. Wang, J., Liu, C., Hussain, I., Li, C., Li, J., Sun, X., Shen, J., Han, W., Wang, L. (2016). Iron-copper bimetallic nanoparticles supported on hollow mesoporous silica spheres: The effect of Fe/Cu ratio on heterogeneous Fenton degradation of a dye. RSC Advances, 6(59), 54623–54635. https://doi.org/10.1039/c6ra08501f
37. Huo, Y., Ding, W., Huang, X., Xu, J., & Zhao, M. (2011). Fluoride removal by lanthanum alginate bead: Adsorbent characterization and adsorption mechanism. Chinese Journal of Chemical Engineering, 19(3), 365–370. https://doi.org/10.1016/S1004-9541(09)60222-6
38. Kumar, A., Rana, A., Sharma, G., Naushad, M., Dhiman, P., Kumari, A., & Stadler, F. J. (2019). Recent advances in nano-Fenton catalytic degradation of emerging pharmaceutical contaminants. Journal of Molecular Liquids, 290, 111177. https://doi.org/10.1016/j.molliq.2019.111177
39. Sun, S., Yang, X., Zhang, Y., Zhang, F., Ding, J., Bao, J., & Gao, C. (2012). Enhanced photocatalytic activity of sponge-like ZnFe2O4 synthesized by solution combustion method. Progress in Natural Science: Materials International, 22(6), 639–643. https://doi.org/10.1016/j.pnsc.2012.11.008
40. Ullah, R., Deb, B. K., Yousuf, M., & Mollah, A. (2014). Synthesis and Characterization of Silica Coated Iron-Oxide Composites of Different Ratios. International Journal of Composite Materials, 4(2), 135–145. https://doi.org/10.5923/j.cmaterials.20140402.13
41. Yu, J., Jin, J., Cheng, B., & Jaroniec, M. (2014). A noble metal-free reduced graphene oxide-cds nanorod composite for the enhanced visible-light photocatalytic reduction of CO2 to solar fuel. Journal of Materials Chemistry A, 2(10), 3407–3416. https://doi.org/10.1039/c3ta14493c
42. Muhammad, W., Ullah, N., Haroon, M., & Abbasi, B. H. (2019). Optical, morphological and biological analysis of zinc oxide nanoparticles (ZnO NPs) using: Papaver somniferum L. RSC Advances, 9(51), 29541–29548. https://doi.org/10.1039/c9ra04424h
43. Yedurkar, S., Maurya, C., & Mahanwar, P. (2016). Biosynthesis of Zinc Oxide Nanoparticles Using Ixora Coccinea Leaf Extract—A Green Approach. Open Journal of Synthesis Theory and Applications, 05(01), 1–14. https://doi.org/10.4236/ojsta.2016.51001
44. Wang, P., Wang, X., Yu, S., Zou, Y., Wang, J., Chen, Z., Alharbi, S. N., Alsaedi, A., Hayat, T., Chen, Y., & Wang, X. (2016). Silica coated Fe 3 O 4 magnetic nanospheres for high removal of organic pollutants from wastewater. Chemical Engineering Journal, 306, 280–288. https://doi.org/10.1016/j.cej.2016.07.068
45. Konicki, W., Sibera, D., Mijowska, E., Lendzion-Bieluń, Z., & Narkiewicz, U. (2013). Equilibrium and kinetic studies on acid dye Acid Red 88 adsorption by magnetic ZnFe2O4 spinel ferrite nanoparticles. Journal of colloid and interface science, 398, 152–60. https://doi.org/10.1016/j.jcis.2013.02.021
46. Kragović, M., Stojmenović, M., Petrović, J., Loredo, J., Pašalić, S., Nedeljković, A., & Ristović, I. (2019). Influence of Alginate Encapsulation on Point of Zero Charge (pHpzc) and Thermodynamic Properties of the Natural and Fe(III) - Modified Zeolite. Procedia Manufacturing, 32, 286–293. https://doi.org/10.1016/j.promfg.2019.02.216
47. Banerjee, S., & Chattopadhyaya, M. C. (2017). Adsorption characteristics for the removal of a toxic dye, tartrazine from aqueous solutions by a low cost agricultural by-product. Arabian Journal of Chemistry, 10, S1629–S1638. https://doi.org/10.1016/j.arabjc.2013.06.005
48. Musa, M., Hasan, H., Malkoç, H., Ergüt, M., Uzunoğlu, D., & Özer, A. (2020). Effective adsorption of tetracycline with Co_3O_4/Fe_3O_4 bimetallic nanoparticles. Turkish Journal of Engineering, 4(4), 209-217. https://doi.org/10.31127/tuje.648882
49. Meena, A. K., Kadirvelu, K., Mishraa, G. K., Rajagopal, C., & Nagar, P. N. (2008). Adsorption of Pb(II) and Cd(II) metal ions from aqueous solutions by mustard husk. Journal of Hazardous Materials, 150(3), 619–625. https://doi.org/10.1016/j.jhazmat.2007.05.011
50. Eltaweil, A. S., Ali Mohamed, H., Abd El-Monaem, E. M., & El-Subruiti, G. M. (2020). Mesoporous magnetic biochar composite for enhanced adsorption of malachite green dye: Characterization, adsorption kinetics, thermodynamics and isotherms. Advanced Powder Technology, 31(3), 1253–1263. https://doi.org/10.1016/j.apt.2020.01.005
51. Chinthalapudi, N., Kommaraju, V. V. D., Kannan, M. K., Nalluri, C. B., & Varanasi, S. (2021). Composites of cellulose nanofibers and silver nanoparticles for malachite green dye removal from water. Carbohydrate Polymer Technologies and Applications, 2, 100098. https://doi.org/10.1016/j.carpta.2021.100098
52. Sarojini, G., Venkatesh Babu, S., Rajamohan, N., & Rajasimman, M. (2022). Performance evaluation of polymer-marine biomass based bionanocomposite for the adsorptive removal of malachite green from synthetic wastewater. Environmental Research, 204, 112132. https://doi.org/10.1016/j.envres.2021.112132
53. Hojjati-Najafabadi, A., Nasr Esfahani, P., Davar, F., Aminabhavi, T. M., & Vasseghian, Y. (2023). Adsorptive removal of malachite green using novel GO@ZnO-NiFe2O4-αAl2O3 nanocomposites. Chemical Engineering Journal, 471(May), 144485. https://doi.org/10.1016/j.cej.2023.144485
54. Hashem, A. A., Mahmoud, S. A., Geioushy, R. A., & Fouad, O. A. (2023). Adsorption of malachite green dye over synthesized calcium silicate nanopowders from waste materials. Materials Science and Engineering: B, 295(December 2022), 116605. https://doi.org/10.1016/j.mseb.2023.116605
55. Rajabi, M., Mirza, B., Mahanpoor, K., Mirjalili, M., Najafi, F., Moradi, O., Sadegh, H., Shahryari-ghoshekandi, H. R., Asif, M., Tyagi, I., Agarwal, S., Gupta, V. K. (2016). Adsorption of malachite green from aqueous solution by carboxylate group functionalized multi-walled carbon nanotubes: Determination of equilibrium and kinetics

parameters. Journal of Industrial and Engineering Chemistry, 34, 130–138. https://doi.org/10.1016/j.jiec.2015.11.001

56. Haounati, R., Ouachtak, H., El Haouti, R., Akhouairi, S., Largo, F., Akbal, F., Benlhachemi, A., Jada, A., Addi, A. A. (2021). Elaboration and properties of a new SDS/CTAB@Montmorillonite organoclay composite as a superb adsorbent for the removal of malachite green from aqueous solutions. Separation and Purification Technology, 255(2020), 117335. https://doi.org/10.1016/j.seppur.2020.117335
57. Li, X. Y., Wang, W. R., Xue, R. C., Chen, P. Y., Wang, Y., & Yu, L. P. (2023). Carbon dots/silica nanoaggregates for highly efficient adsorption of alizarin red S and malachite green dyes. New Journal of Chemistry, 47(18), 8965–8973. https://doi.org/10.1039/d3nj01273e
58. Langmuir, I. (1918). The adsorption of gases on plane surfaces of glass, mica and platinum. Journal of the American Chemical Society, 40(9), 1361–1403. https://doi.org/10.1021/ja02242a004
59. Freundlich, H. (1907). Über die Adsorption in Lösungen. Zeitschrift für Physikalische Chemie, 57U(1), 385–470. https://doi.org/10.1515/zpch-1907-5723
60. You, X., Zhou, R., Zhu, Y., Bu, D., & Cheng, D. (2022). Adsorption of dyes methyl violet and malachite green from aqueous solution on multi-step modified rice husk powder in single and binary systems: Characterization, adsorption behavior and physical interpretations. Journal of Hazardous Materials, 430, 128445. https://doi.org/10.1016/j.jhazmat.2022.128445
61. Wang, D., Liu, L., Jiang, X., Yu, J., & Chen, X. (2015). Adsorption and removal of malachite green from aqueous solution using magnetic β-cyclodextrin-graphene oxide nanocomposites as adsorbents. Colloids and Surfaces A: Physicochemical and Engineering Aspects, 466, 166–173. https://doi.org/10.1016/j.colsurfa.2014.11.021
62. Vergis, B. R., Hari Krishna, R., Kottam, N., Nagabhushana, B. M., Sharath, R., & Darukaprasad, B. (2018). Removal of malachite green from aqueous solution by magnetic CuFe2O4 nano-adsorbent synthesized by one pot solution combustion method. Journal of Nanostructure in Chemistry, 8(1), 1–12. https://doi.org/10.1007/s40097-017-0249-y
63. Dastkhoon, M., Ghaedi, M., Asfaram, A., Goudarzi, A., Langroodi, S. M., Tyagi, I., Agarwall, S., & Gupta, V. K. (2015). Ultrasound assisted adsorption of malachite green dye onto ZnS:Cu-NP-AC: Equilibrium isotherms and kinetic studies - Response surface optimization. Separation and Purification Technology, 156, 780–788. https://doi.org/10.1016/j.seppur.2015.11.001
64. Chen, H., Liu, T., Meng, Y., Cheng, Y., Lu, J., & Wang, H. (2020). Novel graphene oxide/aminated lignin aerogels for enhanced adsorption of malachite green in wastewater. Colloids and Surfaces A: Physicochemical and Engineering Aspects, 603, 125281. https://doi.org/10.1016/j.colsurfa.2020.125281
65. Tanyol, M. (2017). Rapid malachite green removal from aqueous solution by natural zeolite: Process optimization by response surface methodology. Desalination and Water Treatment, 65, 294–303. https://doi.org/10.5004/dwt.2017.20185
66. Hameed, B. H., & El-Khaiary, M. I. (2008). Malachite green adsorption by rattan sawdust: Isotherm, kinetic and mechanism modeling. Journal of Hazardous Materials, 159(2–3), 574–579. https://doi.org/10.1016/j.jhazmat.2008.02.054
67. Sadegh, H., Shahryari-Ghoshekandi, R., Agarwal, S., Tyagi, I., Asif, M., & Gupta, V. K. (2015). Microwave-assisted removal of malachite green by carboxylate functionalized multi-walled carbon nanotubes: Kinetics and equilibrium study. Journal of Molecular Liquids, 206, 151–158. https://doi.org/10.1016/j.molliq.2015.02.007
68. Mohammadi, A., Daemi, H., & Barikani, M. (2014). Fast removal of malachite green dye using novel superparamagnetic sodium alginate-coated Fe_3O_4 nanoparticles. International Journal of Biological Macromolecules, 69, 447–455. https://doi.org/10.1016/j.ijbiomac.2014.05.042
69. Ali, H., & Ismail, A. M. (2021). Developing montmorillonite/PVDF/PEO microporous membranes for removal of malachite green: adsorption, isotherms, and kinetics. Journal of Polymer Research, 28(11), 429. https://doi.org/10.1007/s10965-021-02789-3
70. Ghaedi, M., Azad, F. N., Dashtian, K., Hajati, S., Goudarzi, A., & Soylak, M. (2016). Central composite design and genetic algorithm applied for the optimization of ultrasonic-assisted removal of malachite green by ZnO Nanorod-loaded activated carbon. Spectrochimica Acta - Part A: Molecular and Biomolecular Spectroscopy, 167, 157–164. https://doi.org/10.1016/j.saa.2016.05.025
71. Lagergren, S. K. (1898). About the Theory of So-called Adsorption of Soluble Substances. Sven. Vetenskapsakad. Handingarl, 24, 1–39.
72. Ho, Y. S., & McKay, G. (2004). Sorption of copper(II) from aqueous solution by Peat. Water, Air, and Soil Pollution, 158(1), 77–97. https://doi.org/10.1023/B:WATE.0000044830.63767.a3
73. Weber, W. J., & Morris, J. C. (1963). Closure to "Kinetics of Adsorption on Carbon from Solution". Journal of the Sanitary Engineering Division, 89(6), 53–55. https://doi.org/10.1061/jsedai.0000467